Electrochemical Impedance Evaluation of Paper-based Glucose Biofuel Cell

Isao Shitanda,* Kazuhiro Ishigoori, Noya Loew,
Hikari Watanabe, and Masayuki Itagaki

Department of Pure and Applied Chemistry, Faculty of Science and Technology, Tokyo University of Science,
2641, Yamazaki, Noda, Chiba 278-8510, Japan

Paper-based biofuel cells have the potential to serve as health monitoring devices for urinary glucose and volume by incorporating the fabricated electrodes into nursing diapers. In this study, we evaluate the output power and stability of a biofuel cell by combining 3D impedance measurement and admittance analysis. The 3D impedance-based analysis method can simultaneously detect changes in the overall electrode structure of the enzyme electrode and in the quantity of active enzymes and mediators on the electrode surface. The biofuel cell electrodes were fabricated via screen-printing, using polydimethylglycidyl (poly-GMA)-modified MgO-templated carbon (GMgOC) or poly-GMA-unmodified MgO-templated carbon (NMgOC). The enzymes used were flavin adenine dinucleotide-dependent glucose dehydrogenase and bilirubin oxidase, with Azure-A serving as the mediator. Admittance analysis was utilized to measure the enzyme activity and estimate the charge transfer resistance by extrapolating the spectra obtained through admittance analysis. The charge transfer resistances of both electrodes exhibited a greater stability for the GMgOC electrode. This can be attributed to the covalent immobilization of the enzyme and mediator on the electrode facilitated by GMgOC, effectively suppressing enzyme and mediator elution. The electric double-layer capacitance values of both electrodes indicated the overall stability of the electrode structure during the measurement.

1. Introduction

In recent years, methods used to evaluate health conditions rapidly and in real time have attracted considerable attention; wearable devices offer a solution to these requirements, leading to efforts to develop devices that do not cause stress or discomfort to patients.[1,2]

Wearable devices are worn on the body to monitor the health status by measuring components in bodily fluids such as sweat, tears, urine, and saliva, and have been implemented as alternatives to blood tests. The sampling of bodily fluids is noninvasive, as opposed to the invasive sampling

---

*Corresponding author: e-mail: shitanda@rs.tus.ac.jp

of blood.[3–7] In particular, urinary glucose concentrations have the additional advantages of correlating with blood glucose concentrations[8,9] and being higher than those in saliva or tears. Urinary glucose is detected when the blood glucose levels exceed the renal threshold ($\geq$10 mmol dm^{-3}). Therefore, the detection of changes in urinary glucose concentration is important for the monitoring, treatment, and prevention of diabetes. The ability to diagnose diabetes at home and share this information with physicians will lead to an improved quality of daily life and an optimal treatment of the disease. These advantages can help prevent the risk of early mortality.

Biofuel cells have attracted attention as a potential source of electric power for wearable diagnostic devices. A biofuel cell is a type of fuel cell that converts the chemical energy of a compound into electrical energy using biocatalysts (enzymes) as electrocatalysts. As such, biofuel cells can generate electricity under mild ecological conditions, including normal temperature, normal pressure, and neutral pH.[10] Enzyme-based biofuel cells are useful power sources for wearable devices because they use enzymes as biocatalysts and substrates contained in bodily fluids as fuel to generate electricity. As the power obtained correlates with the concentration of the components in the bodily fluid, the device can be implemented as self-powered wearable biosensors that can generate power and monitor health conditions simultaneously.

In recent years, the use of porous electrode materials has significantly increased the power output of biofuel cells.[11–13] Among various porous carbon materials, magnesium oxide (MgO)-templated carbon (MgOC) offers the advantage of a large specific surface area and controllable pore size. Tsujimura *et al*. implemented 2,2′-azino-bis(3-ethylbenzothiazolin-6-sulfonate) (ABTS) as a mediator and bilirubin oxidase (BOD) as a biocatalyst on an electrode using MgOC, and successfully obtained a catalytic reduction current of −13.5 mA cm^{-2}.[11] Recently, patch-type lactate biofuel cells have been developed, as reported by Chen *et al*. who developed a stretchable and flexible lactate/oxygen biofuel cell using a Buckypaper.[12] They immobilized enzymes in a pyrene-polynorbornene homopolymer, obtaining a maximum output power of 450 μW.

Our group has been developing biosensing devices that can be easily and inexpensively fabricated, mainly by screen-printing.[13–15] For example, we developed a screen-printed self-powered, wireless biosensor for the monitoring of glucose in urine, which can be integrated into nursing diapers.[14] However, the stability of biosensing devices requires improvement. To effectively improve the stability, first, the reason for the instability must be investigated and quantified. We have recently applied 3D electrochemical impedance spectroscopy (EIS) to distinguish between performance loss due to changes in electrode structure and performance loss due to the leaching of the enzyme and/or mediator.[16]

EIS is a method of characterizing electrochemical systems by applying a small AC potential or current signal to the measurement system and obtaining the impedance of the system. The impedance is determined by various factors such as the diffusion, migration, and convection of electrolytes in solution, the electrode geometry, and the charge transfer reaction mechanism. These factors have different time constants and thus affect the impedance at different AC input signal frequencies.

In general, performing an accurate EIS analysis requires a steady-state measurement system that does not confuse the frequency-dependent changes with time-dependent impedance changes. However, bioelectrodes with stability problems create a non-steady-state system that results in time-dependent impedance changes, rendering ordinary EIS measurements unsuitable for evaluating their stability. To overcome this problem, 3D EIS is used, in which EIS is measured as a function of not only frequency but also time.[16,17] From these data, EI spectra at specific time points are extrapolated.

At times, the apex frequency of impedance spectra may not be observable within reasonably measurable frequencies, which introduces complexity to the evaluation process. In such cases, admittance spectra are employed as they make the apex frequency visible. Admittance represents the reciprocal of impedance. We previously proposed a method that uses admittance analysis to evaluate the resistance of passive films formed on steel bars. Through simulations and its application to real structures, we characterized the corrosion environment of steel bars embedded in concrete.[18]

In this study, we propose a novel method that combines 3D impedance measurements and admittance analysis to evaluate the stability of paper-based porous enzyme electrodes. With this new approach, impedance spectra at various time intervals were determined, and appropriate models were used to fit the obtained curves. This method allows for the evaluation of operational stability and electrode structure modifications involving enzymes and mediators by monitoring time-dependent variations in charge transfer resistance and bilayer capacitance.

2.   Data, Materials, and Methods

2.1   Materials

Japanese paper was obtained from Togawa Seishi Co. The crosslinking agents Neoseed (NR-158) and NK Assist (NY-50) were purchased from NICCA Chemical Co., Ltd. Polyvinylidene fluoride (PVDF, #9305) was obtained from Kureha Corporation. 1-methyl-2-pyrrolidone (NMP) was purchased from FUJIFILM Wako Pure Chemicals Co. MgO-templated carbon (MgOC, CNovel®) was obtained from Toyo Tanso Co. and used as is as nongrafted MgOC (NMgOC). Grafted MgOC (GMgOC) was prepared according to a previous study.[19] Carbon paste (JELCON CH-10) was obtained from Jujo Chemical Co., Ltd. Azure A chloride was obtained from Sigma-Aldrich, Japan. Flavin adenine dinucleotide-glucose dehydrogenase (FAD-GDH) and bilirubin oxidase (BOD) were purchased from Amano Enzyme Inc. (Japan). All the chemicals were of analytical grade.

2.2   Fabrication of screen-printed enzyme electrodes

Prior to printing, the Japanese paper was subjected to a treatment involving the application of a water repellent followed by a drying period of 24 h. To create the water repellent solution,

NeoSeed and NK Assist were diluted 100 and 500 times, respectively, using pure water. These diluted solutions were then combined in a volume ratio of 20:3, mixing NeoSeed with NK Assist. Next, five layers of the carbon paste were screen-printed on the water-repellent-treated paper substrate as the leads and dried at 120 °C for 24 h. Subsequently, two layers of NMgOC or GMgOC porous carbon ink were screen-printed on the leads. The porous carbon ink composed of 1.0 g of porous carbon, 7.0 mL of PVdF as a binder, and 4.8 mL of NMP as a solvent was prepared according to a previous report.[13,17] The surface area of the electrode was 1.0 cm^2 (0.5 cm × 2.0 cm).

Before modification, the electrode was treated with ultraviolet (UV)-ozone for 15 min to remove impurities from its surface. An enzyme solution was prepared by dissolving the enzyme in 10 mmol dm^{-3} phosphate buffer with a pH of 7.0. To fabricate the bioanode, 10 μL cm^{-2} of supersaturated Azure A in methanol was drop-casted onto the electrode and dried under vacuum for 30 min, followed by 20 μL cm^{-2} of FAD-GDH in 10 mmol dm^{-3} phosphate buffer and drying under reduced pressure for 1 h. To prepare the biocathode, 20 μL cm^{-2} of BOD in 10 mmol dm^{-3} phosphate buffer was drop-casted and dried under vacuum for 1 h.

2.3   Electrochemical measurement

Single-electrode cyclic voltammetry measurements were conducted in a three-electrode system using the porous carbon electrode as the working electrode (WE), a saturated KCl silver/silver chloride electrode as the reference electrode (RE), and a Pt wire as the counter electrode (CE). Cyclic voltammetry (CV) was measured at a scan rate of 10 mV/s. Full-cell linear-sweep voltammetry measurements were performed using the bioanode and a biocathode in a two-electrode biofuel cell (Fig. 1).

The impedance measurements were carried out in a two-part acrylic cell (Fig. 2). The carbon WE was sandwiched between the two parts. A cylindrical chamber in the middle of the assembled cell contained the electrolyte. A hole at the top of the cell was used to insert the reference electrode, and another hole to insert the counter electrode. Oxygen is supplied from the back of the working electrode through an inlet.
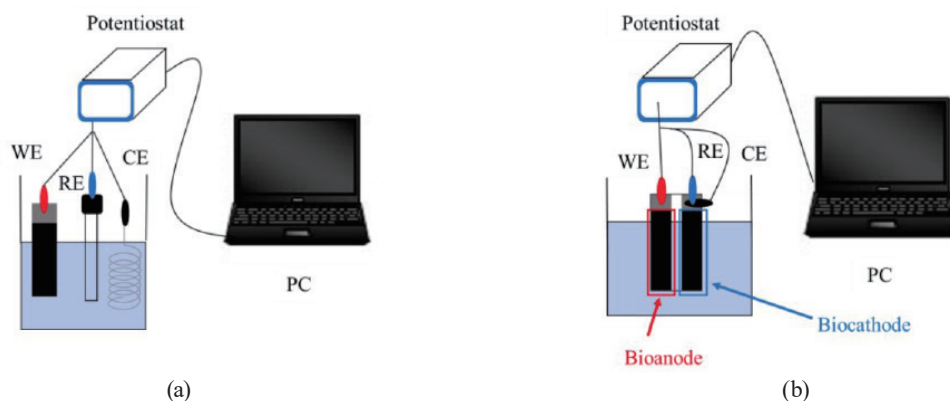

| (a) | (b) |

Fig. 1.   (Color online) Measurement setup for (a) single-electrode cyclic and (b) full-cell linear-sweep voltammetry measurements.
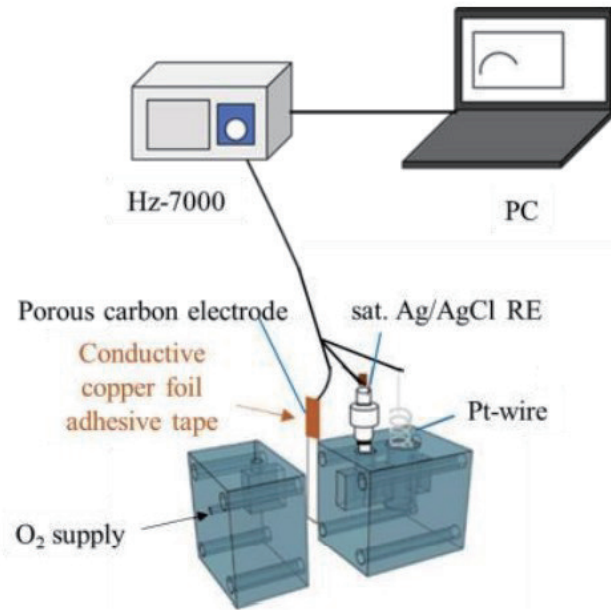
Fig. 2.   (Color online) Setup for impedance measurements.

The 3D impedance measurements were performed with an applied current of 100 µA and a current amplitude of 25 µA in the frequency range from 10 kHz to 10 mHz with five measurement points per order of magnitude. A potentiostat (Hz-7000, Hokuto Denko Co., Ltd.) with a built-in frequency response analyzer was used for the measurements. A 1.0 M phosphate buffer solution (pH 7.0) was used as the electrolyte. The measurements were performed in an environmental chamber at 36.5 °C and 70% humidity.

2.4.   Equivalent circuit for EIS analysis

Figure 3 shows the equivalent circuit used to fit the obtained impedance spectra, where R_{sol} (Ω) represents the solution resistance, R_{ct} (Ω) is the charge transfer resistance, and CPE is a constant phase element.

Figure 4(a) shows an example of a Nyquist plot where the vertex frequency is not visible in the low-frequency region of the spectrum (the data in the example were measured 2 h after the start of the experiment). In this case, by admittance analysis [Fig. 4(b)], we observe that the low-frequency side converges and that the charge transfer resistance R_{ct} is determined.

From the equivalent circuit (Fig. 3), the electrochemical impedance Z, its real component Z′, and its imaginary component Z″ can be elucidated as Eqs. (1)–(3), respectively. Here, T_{CPE} ($\Omega^{p-1}F^p$) is the CPE constant, p is the CPE exponent, j is the imaginary unit, and ω (rad s^{-1}) is the angular frequency. As the admittance Y is the reciprocal of Z, its real component Y′ and its imaginary component Y″ can be expressed as Eqs. (4), and (5), respectively. By elucidating the high-frequency ($\omega \rightarrow \infty$) and low-frequency ($\omega \rightarrow 0$) limits for Z′ and Z″ from Eqs. (2) and (3), and substituting them into Eqs. (4) and (5), the limits for Y′ and Y″ can be calculated as Eqs. (6)
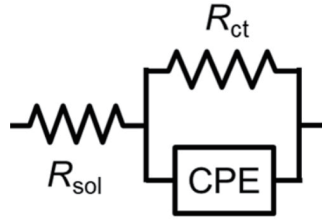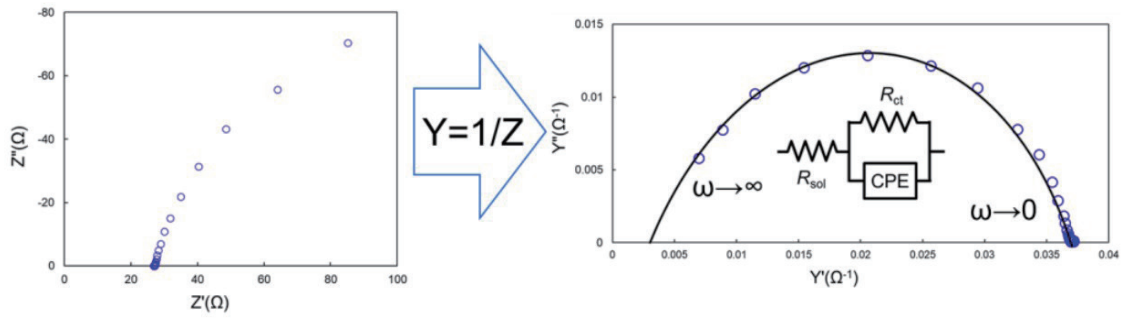
Fig. 3.   Equivalent circuit used.

Fig. 4.   (Color online) Example of vertex frequency not being visible. (a) Nyquist plot. (b) Admittance plot.

and (7), respectively. Thus, by extrapolating, R_{ct} and R_{sol} can be determined from the admittance plot. With these values and Eqs. (1) to (3), T_{CPE} and p can be calculated. Furthermore, the electric double-layer capacitance C_{dl} (F) is given by Eq. (8) and can be calculated using the obtained parameter values.

$$Z = R_{sol} + \frac{R_{ct}}{1+(j\omega)^p T_{CPE} R_{ct}} \tag{1}$$

$$Z = R_{sol} + \frac{R_{ct}\left\{1+\omega^p T_{CPE} R_{ct}\cos\left(\frac{\pi}{2}p\right)\right\}}{1+2\omega^p T_{CPE} R_{ct}\cos\left(\frac{\pi}{2}p\right)+\omega^{2p} T_{CPE}^2 R_{ct}^2} \tag{2}$$

$$Z'' = \frac{\omega^p T_{CPE} R_{ct}^2 \sin\left(\frac{\pi}{2}p\right)}{1+2\omega^p T_{CPE} R_{ct}\cos\left(\frac{\pi}{2}p\right)+\omega^{2p} T_{CPE}^2 R_{ct}^2} \tag{3}$$

$$Y' = \frac{Z'}{Z'^2 + Z''^2} \tag{4}$$

$$Y^{\bullet} = \frac{Z^{\bullet}}{Z^2 + Z^{\bullet 2}} \qquad (5)$$

$$Y'_{\omega \to \infty} = \frac{1}{R_{sol}} \qquad (6)$$

$$Y'_{\omega \to 0} = \frac{1}{R_{sol} + R_{ct}} \qquad (7)$$

$$C_{dl} = \left(T_{CPE} / R_{ct}{}^{\rho-1} \right)^{1/\rho} \qquad (8)$$

3.   Results and Discussion

In our previous study,[14] a small amount of surfactant was utilized to facilitate the entry of the enzyme solution into the electrode's pores during the immobilization of enzymes. However, in this particular study, no surfactant was utilized. First, the amount of enzyme modification of the biocathode was optimized. For this, the cyclic voltammetry of biocathodes was performed using GMgOC as the electrode material and modified by varying the amount of enzyme (Fig. 5). Figure 5(b) shows the catalytic current (Δi) for each enzyme amount at -0.2 V (vs Ag/AgCl). Δi is the maximum current density for each enzyme amount minus the maximum current density without the enzyme (background). From the results in Fig. 5, the optimal enzyme quantity for the biocathode using the GMgOC electrode was determined to be 20 U cm^{-2}. Subsequently, biocathodes were modified with 20 U cm^{-2} each.

Next, the stabilities of biocathodes with NMgOC and GMgOC were compared using cyclic voltammetry (Figs. 6 and 7). Figure 6 shows that the GMgOC electrode had a lower current
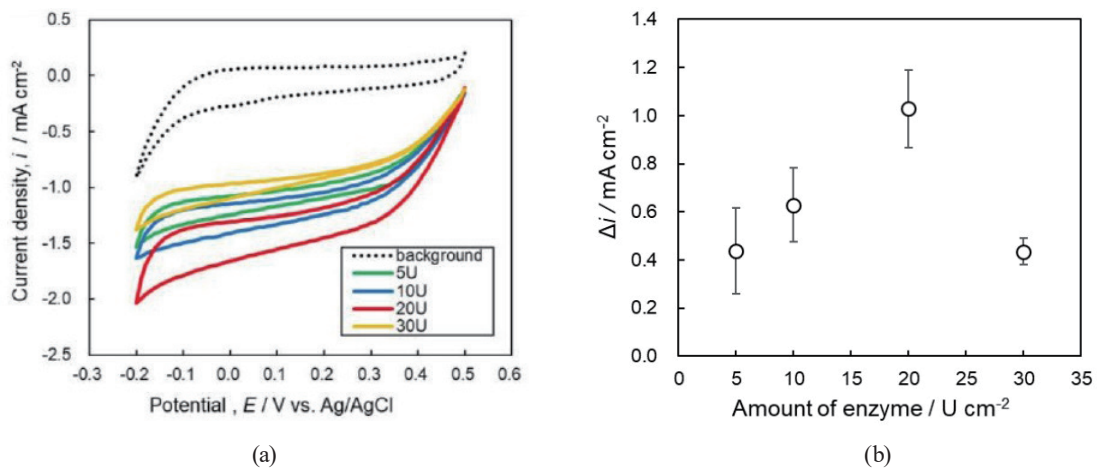

(a)   (b)

Fig. 5.   (Color online) Examination of amount of enzyme modification: (a) CV and (b) Δi for each amount of enzyme modification (90% confidence interval).
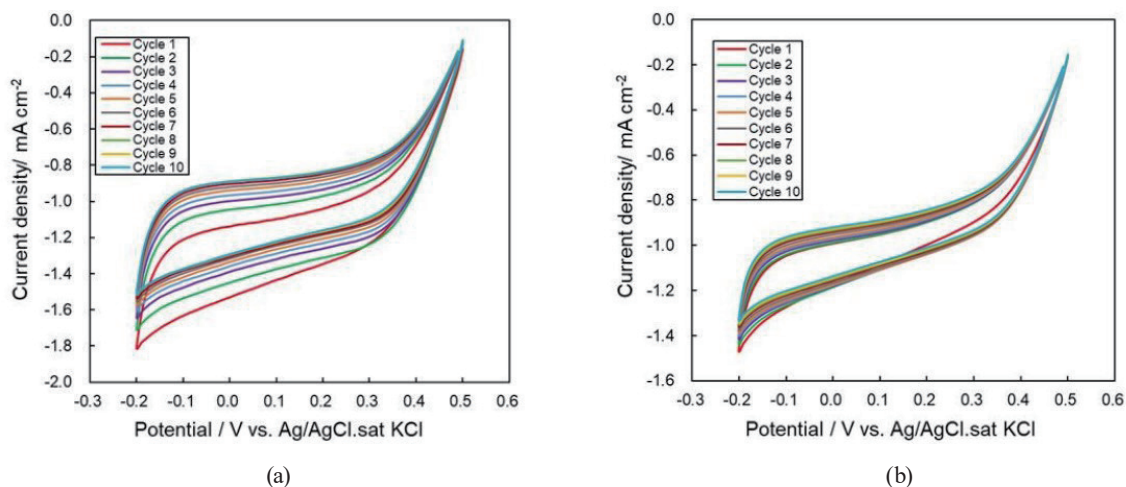
Fig. 6.   (Color online) Ten cycles of CV for the (a) NMgOC and (b) GMgOC biocathodes.
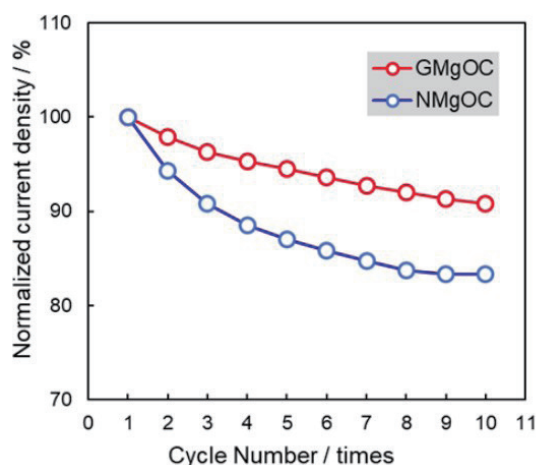

Fig. 7.   (Color online) Current retention for 10 cycles for GMgOC and NMgOC biocathodes. Normalized current densities at −0.2 V from CV measurements (Fig. 6.).

density than the NMgOC electrode in the first cycle. The biocathodes in this study rely on a direct electron transfer mechanism between the BOD and the electrode. In the NMgOC electrode, the BOD is adsorbed directly on the carbon surface. In the GMgOC electrode, the BOD is immobilized via a polymer chain on the surface of the carbon electrode. As such, there is a larger average distance between the electrode surface and the BOD in general, and thus, the T1 copper is in its active center, which accepts electrons from the electrode. This leads to the lower current density of the GMgOC electrode observed in the first cycle of cyclic voltammetry (Fig. 6).

However, it is apparent that the GMgOC electrode is significantly more stable than the NMgOC electrode. Figure 7 shows that after 10 CV cycles, the current retention was higher for the GMgOC electrode than for the NMgOC electrode. This improved stability can be attributed to the covalent immobilization of the BOD on the GMgOC electrode being more stable than the immobilization by physical adsorption on the NMgOC electrode.

The GMgOC and NMgOC biocathodes were paired with their respective bioanodes to construct biofuel cells. The GMgOC electrode exhibited a slightly higher output than the NMgOC electrode (Fig. 8). The GMgOC-based biofuel cell achieved a maximum power density of 0.62 mW cm^{-2} and a maximum current density of 1.39 mA cm^{-2}. This represents a fivefold increase in power compared with our previous biofuel cell/self-powered diaper sensor,[14] suggesting that the surfactant used in the previous study had more adverse effects than benefits.

Stability evaluations of the bioanode can be conducted, as demonstrated in similar studies.[14,19,20] However, since stability evaluations using CV were not the focus of this study, the evaluations were limited to the biocathode.

While it can be inferred that the difference in stability between the GMgOC and NMgOC electrodes is due to the enzyme immobilization, the above results (Figs. 6 and 7) do not prove this conclusion. 3D EIS can be employed to distinguish between stability differences due to the loss of the active enzyme from differences in general electrode structure.[16]

Furthermore, CV measurements are unsuitable for assessing stability over a large time scale. Additionally, during CV measurements, the electrode remains at non-operating potentials for the majority of the time, potentially causing artificial electrode reactions that exaggerate instabilities. In contrast, 3D EIS overcomes these limitations associated with CV measurements. It enables measurements to be taken over an extended period, even throughout the entire electrode lifetime, and can be performed under conditions that closely resemble operating conditions, minimizing the likelihood of measuring artificial instabilities.

Therefore, in this study, we utilized 3D EIS to evaluate the stabilities of the fabricated bioanodes and biocathodes. The 3D EIS measurements were conducted under controlled current conditions, which approximate operating conditions better than controlled potential conditions. The 3D Nyquist plots of the bioanode and biocathode (Figs. 9 and 10, respectively) were interpolated at specific time points and converted into admittance plots. From these plots, the relevant R_{ct} (charge-transfer resistance) and C_{dl} (double-layer capacitance) values were determined, following the methodology outlined in the methods section.
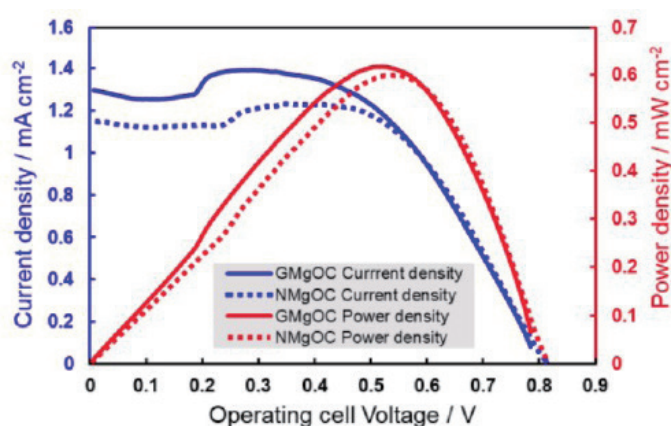

Fig. 8.   (Color online) Current and power output of biofuel cell with FAD-GDH/azure A bioanode and BOD biocathode.
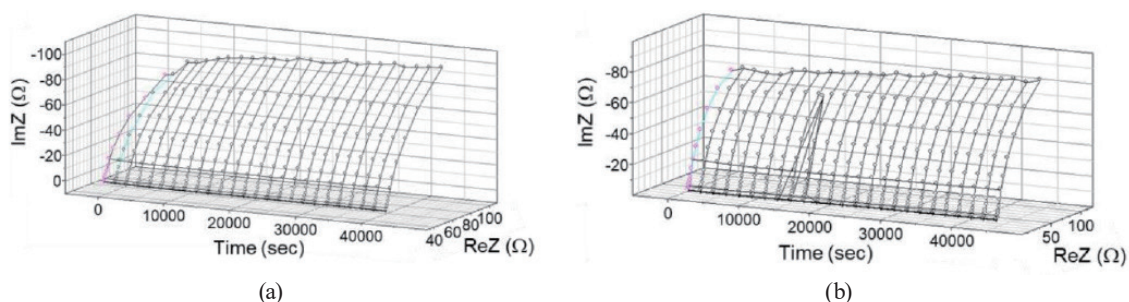
(a)   (b)

Fig. 9.   (Color online) 3D Nyquist plot of a bioanode fabricated with (a) NMgOC and (b) GMgOC.

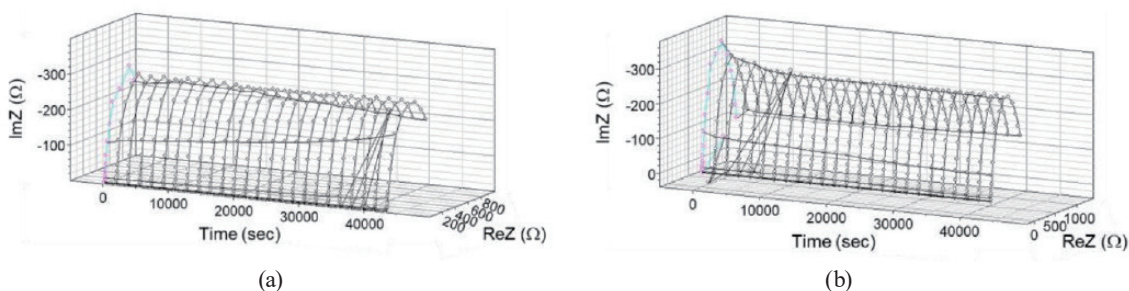(a)   (b)

Fig. 10.   (Color online) 3D Nyquist plot of a biocathode fabricated with (a) NMgOC and (b) GMgOC.

C_{dl} serves as an indicator of the effective surface area of the electrode and, consequently, the overall electrode structure. Thus, we investigated its time dependence (Fig. 11). Notably, the C_{dl} value of the NMgOC electrode exceeded that of the GMgOC electrode for both the bioanode and the biocathode. This disparity can be attributed to the covalent bonding of poly-GMA on the surface of the GMgOC electrode, resulting in a smaller effective surface area available for the electrode reaction. Furthermore, the C_{dl} value remained constant over extended periods of time for both the GMgOC and NMgOC electrodes, as well as for both the bioanode and the biocathode. This constancy suggests that the general structure of the electrodes remained unchanged throughout the measurements.

Furthermore, the C_{dl} value of the bioanode exceeded that of the biocathode. This distinction arises from the different electron transfer mechanisms employed, leading to various effective surface areas. The biocathode utilized a direct electron transfer mechanism, requiring a larger surface area per electron transfer. Conversely, the bioanode employed a mediated electron transfer mechanism, requiring a much smaller surface area per electron transfer. Consequently, given the same surface area, the effective surface area of the biocathode was smaller than that of the bioanode.

R_{ct} serves as an indicator of the efficiency of the electrode reaction. Thus, we investigated its time dependence (Fig. 12). Although R_{ct} increased over time in all cases, the increase was more pronounced for the NMgOC electrode than for the GMgOC electrode, for both the bioanode and the biocathode. The elevated R_{ct} value over time could be attributed to enzyme and/or mediator elution, or enzyme inactivation. The smaller change in R_{ct} observed with the GMgOC electrode validates the enhanced stability, attributed to the covalent immobilization of the enzyme, which impedes elution.
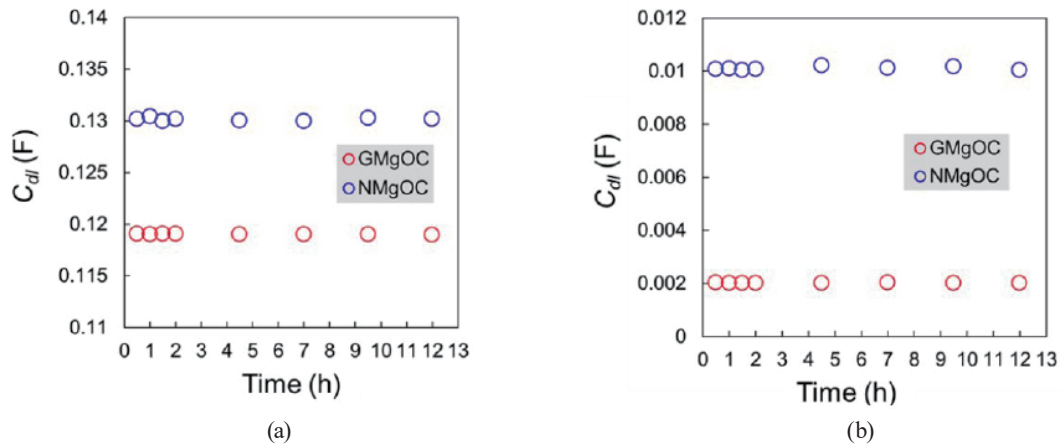
Fig. 11.   (Color online) Change in electric double-layer capacitance C_{dl} over time for (a) bioanode and (b) biocathode.
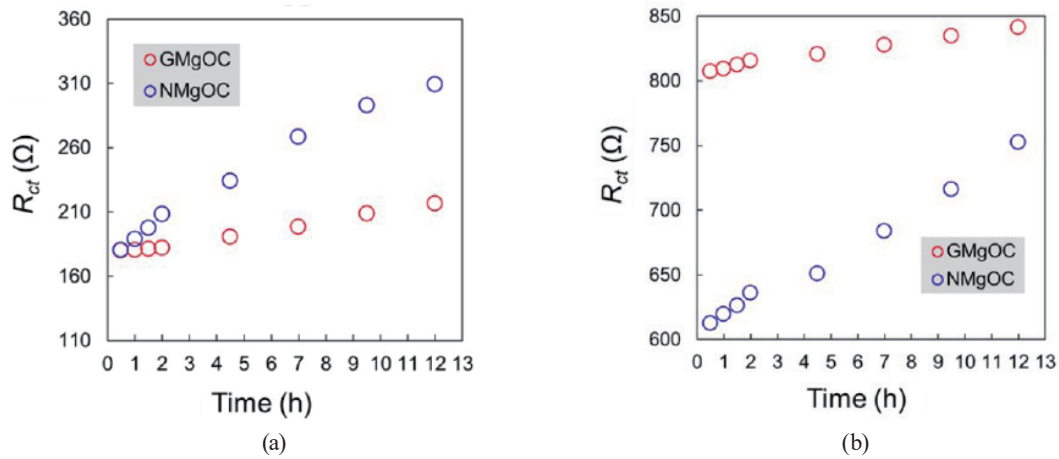

Fig. 12.   (Color online) Change in charge transfer resistance R_{ct} over time for (a) bioanode and (b) biocathode.

Furthermore, while the initial R_{ct} values of the GMgOC and NMgOC bioanodes are similar, the initial R_{ct} value of the GMgOC biocathode is larger than that of the NMgOC biocathode (Fig. 12) and maintains this disparity at all evaluated time points. As mentioned above, the biocathode in this study employs a direct electron transfer principle. The efficiency of direct electron transfer diminishes as the distance between the enzyme's active center and the electrode increases. Hence, the elevated R_{ct} value of the GMgOC biocathode can be attributed to the immobilization of the BOD on the polymer chain present on the surface of the carbon electrode, resulting in a greater distance between the T1 copper of the active center and the electrode surface.

Overall, the results obtained by 3D EIS are in agreement with the results obtained by CV, indicating the validity of 3D EIS evaluation. Compared with CV measurements, 3D EIS evaluation provides more direct evidence and thus can be used in cases where the interpretation of CVs is less clear.

Nevertheless, addressing the discrepancies between the CV and 3D EIS results is essential. From the CV findings, the biocathode appears to stabilize after 20–30 min, particularly when using NMgOC (Fig. 7). However, the 3D EIS results indicate a consistent degradation over a span of at least 12 h [Fig. 12(b)]. This discrepancy could be attributed to either the two-stage elution of the BOD (i.e., a fast elution followed by a slower one) or the rapid, short-lived elution at non-operating potentials and the gradual, continuous elution at operating potentials. Particularly in the latter scenario, 3D EIS measurements provide more realistic data for assessing the stability of biofuel cell electrodes.

4.   Conclusions

In this study, a 3D electrochemical impedance method and admittance analysis were combined to obtain various parameters regarding the electrochemical behavior of biofuel cell electrodes and evaluate their operational stability. Admittance analysis was performed on the measured spectra to obtain the convergence on the low-frequency side.

The NMgOC electrode demonstrated a higher electric double-layer capacitance than the GMgOC electrode throughout the experiment. This disparity can be attributed to the covalent bonding of poly-GMA on the electrode surface, which effectively reduces the effective surface area of the GMgOC electrode. The reason why the electric double-layer capacitance remained constant for the NMgOC and GMgOC electrodes regardless of time is considered to be related to the stability in the electrode structure over time.

Next, the change in charge-transfer resistance was explored, revealing that the GMgOC bioanode showed smaller changes in resistance over time than the NMgOC electrode, suggesting that the GMgOC electrode is more stable in terms of operational stability. The resistance of the GMgOC biocathode was larger than that of the NMgOC electrode at each time point, but the time variation of the value was smaller. We hypothesize that this is because in the case of the GMgOC electrode, the BOD is immobilized on the polymer chains on the surface of the carbon electrode, which increases the electron transfer distance from the electrode surface to the enzyme, resulting in a higher charge transfer resistance than in the case of the NMgOC electrode at the initial stage of the measurement. However, the stability of the GMgOC electrode was higher, resulting in a lower variation over time than in the case of the NMgOC electrode.

Finally, we expect this novel and promising measurement method to be instrumental for the evaluation of biofuel cell performance stability by the simultaneous analysis of bioanodes and biocathodes in the near future.

Acknowledgments

References

1 J. R. Windmiller and J. Wang: Electroanalysis **25** (2013) 29. https://doi.org/10.1002/elan.201200349
2 A. J. Bandodkar, I. Jeerapan, and J. Wang: ACS Sens. **1** (2016) 464. https://doi.org/10.1021/acssensors.6b00250
3 C. Gonzalez-Solino and M. Lorenzo: Biosensors **8** (2018) 11. https://doi.org/10.3390/bios8010011
4 W. Gao, S. Emaminejad, H. Y. Nyein, S. Challa, K. Chen, A. Peck, H. M. Fahad, H. Ota, H. Shiraki, D. Kiriya, D. H. Lien, G. A. Brooks, R. W. Davis, and A. Javey: Nature **529** (2016) 509. https://doi.org/10.1038/nature16521
5 J. Kim, A. S. Campbell, and J. Wang: Talanta **177** (2018) 163. https://doi.org/10.1016/j.talanta.2017.08.077
6 S. Imani, A. J. Bandodkar, A. M. Mohan, R.Kumar, S. Yu, J. Wang, and P. P.Mercier: Nat. Commun. **7** (2016) 11650. https://doi.org/10.1038/ncomms11650
7 J. Kim, A. S. Campbell, B. E.-F. de Ávila, and J. Wang: Nat. Biotechnol. **37** (2019) 389. https://doi.org/10.1038/s41587-019-0045-y
8 P. Sharma and P. Sharan: IEEE Sens. J. **15** (2015) 1035. https://doi.org/10.1109/JSEN.2014.2359799
9 M. Miyashita, N. Ito, S. Ikeda, T. Murayama, K. Oguma, and J. Kimura: Biosens. Bioelectron. **24** (2009) 1336. https://doi.org/10.1016/j.bios.2008.07.072
10 C. Desmet, C. A. Marquette, L. J. Blum, and B. Doumeche: Biosens. Bioelectron. **76** (2016) 14. https://doi.org/10.1016/j.bios.2015.06.052
11 S. Tsujimura, K. Murata, and W. Akatsuka: J. Am. Chem. Soc. **136** (2014) 14432. https://doi.org/10.1021/ja5053736
12 X. Chen, L. Yin, J. Lv, A. J. Gross, M. Le, N. G. Gutierrez, Y. Li, I. Jeerapan, F. Giroud, A. Berezovska, R. K. O'Reilly, S. Xu, S. Cosnier, and J. Wang: Adv. Funct. Mater. **29** (2019) 1905785. https://doi.org/10.1002/adfm.201905785
13 I. Shitanda, Y. Morigayama, R. Iwashita, H. Goto, T. Aikawa, T. Mikawa, Y. Hoshi, M. Itagaki, H. Matsui, S. Tokito, and S. Tsujimura: J. Power Sources **489** (2021) 229533. https://doi.org/10.1016/j.jpowsour.2021.229533
14 I. Shitanda, Y. Fujimura, T. Takarada, R. Suzuki, T. Aikawa, M. Itagaki, and S. Tsujimura: ACS Sens. **6** (2021) 3409. https://doi.org/10.1021/acssensors.1c01266
15 I. Shitanda, M. Momiyama, N. Watanabe, T. Tanaka, S. Tsujimura, Y. Hoshi, and M. Itagaki: ChemElectroChem **4** (2017) 2460. https://doi.org/10.1002/celc.201700561
16 I. Shitanda, H Inoue, Y. Yoshihata, N. Loew, and M Itagaki: Biosens. Bioelectron. **178** (2021) 113014. https://doi.org/10.1016/j.bios.2021.113014
17 Z. B. Stoynov and B. S. Savova-Stoynov: J. Electroanal. Chem. **183** (1985) 133. https://doi.org/10.1016/0368-1874(85)85486-1
18 M. Itagaki, K. Inohira, H. Watanabe, I. Shitanda, S. Namimatsu, R.Kakinouchi, and Y. Hoshi: *Zairyo-to-kankyou* **71** (2022) 13 (in Japanese). https://doi.org/10.3323/jcorr.71.13
19 I. Shitanda, T. Kato, R. Suzuki, T. Aikawa, Y. Hoshi, M. Itagaki, and S. Tsujimura: Bull. Chem. Soc. Jpn. **93** (2020) 32. https://doi.org/10.1246/bcsj.20190212
20 I. Shitanda, M. Mitsumoto, N. Loew, Y. Yoshihara, H. Watanabe, T. Mikawa, S. Tsujimura, M. Itagaki, and M. Motosuke: Electrochim. Acta **368** (2021) 137620. https://doi.org/10.1016/j.electacta.2020.137620